# Conserved Charge Fluctuations from RHIC BES and FXT

Toshihiro Nonaka for the STAR collaboration,

Tomonaga Center for the History of the Universe, University of Tsukuba, Tenno-dai 1-1-1, Tsukuba, Ibaraki, 305-8571, Japan

November 30, 2023

**Abstract**

Cumulants up to the sixth-order of the net-particle multiplicity distributions were measured at RHIC for the Beam Energy Scan and fixed-target program, from which we obtained some interesting hints on the phase structure. In this article, we present recent experimental results on (net-)proton cumulants and discuss current interpretations on the QCD critical point and the nature of the phase transition. We will also report recent attempt for measurements of the bayron-strangeness correlations, which is measured with the newly-developed method to remove the effect from the combinatorial backgrounds for hyperon reconstructions.

## 1 Introduction

One of the ultimate goals in heavy-ion collision experiments is to understand the phase structure of the matter described by Quantum ChromoDynamics (QCD) and the nature of the phase transition. Figure 1 depicts a conjectured phase diagram for the QCD matter [1]

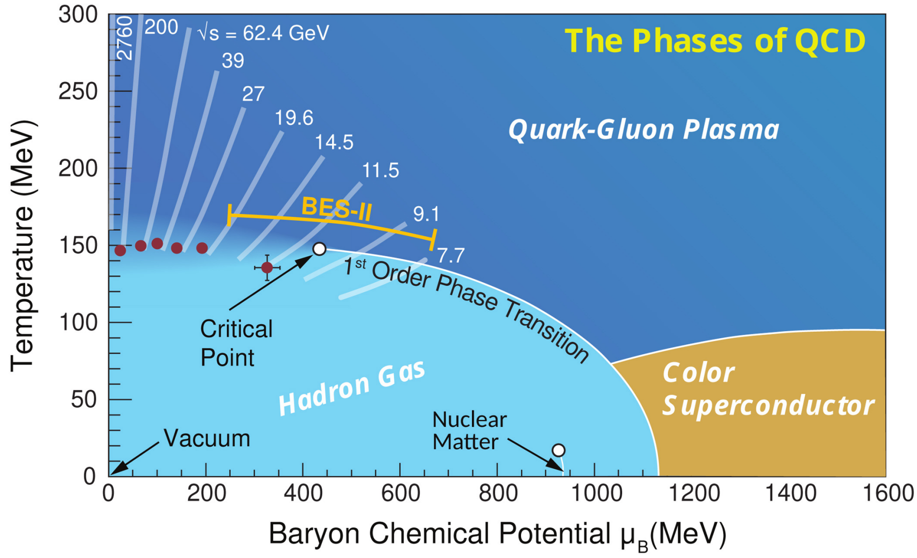


Figure 1: The conjectured QCD phase diagram with respect to the baryon chemical potential and temperature [1]. The energies and ranges represent collision energies from the experimental programs at RHIC and LHC.

with respect to temperature $T$ (MeV) and baryon chemical potential $\mu_{\mathrm{B}}$ (MeV). In the QCD phase diagram, there are two phases of the hadronic gas and quark-gluon plasma (QGP), which are the confined and deconfined states of quarks and gluons, respectively. According to the lattice QCD calculations, the phase transition between QGP and the hadronic gas is a smooth crossover [2] at vanishing baryon chemical potential, $\mu_{\mathrm{B}} = 0$, while model calculations predicts 1st-order phase transition at large $\mu_{\mathrm{B}}$ region [3]. If the 1st-order phase transition exists, the connecting point to the crossover may also exist, which is a QCD critical point.

To explore the QCD phase diagram and elucidate the nature of the phase transition, the Beam Energy Scan (BES-I) program [4] was carried out at RHIC from 2010 to 2017 for Au+Au collisions at $\sqrt{s_{\mathrm{NN}}} = 7.7$, 11.5, 14.5, 19.6, 27, 39, 54.4, 62.4, and 200 GeV. The corresponding baryon chemical potential is around $30 < \mu_{\mathrm{B}} < 400$ MeV, which covers wide region in the QCD phase diagram. The fixed-target (FXT) experiment was also performed for $\sqrt{s_{\mathrm{NN}}} = 3.0$ GeV Au+Au collisions at the STAR detector in 2018, where the baryon chemical potential has been extended up to 720 MeV.

Various observables were measured in BES-I, e.g., conserved charge fluctuations [5, 6, 7, 8] to search for the QCD critical point, directed flow [9] and average transverse mass [10] to search for the fist-order phase transition, elliptic flow [11, 12], nuclear modification factor [13], dynamical charge correlations [14, 15], dileptons [16] to search for the possible boundary of QGP formation. Many of them exhibit interesting trend as a function of the collision energy, but their interpretations have been limited by large uncertainties at low collision energies.

In order to improve those results, the phase II of the BES program (BES-II) was performed in 2019-2021 at $\sqrt{s_{\rm NN}}$ = 7.7, 9.2, 11.5, 13.7, 14.5, 17.3, and 19.6 GeV. The FXT experiments were also carried out at $\sqrt{s_{\rm NN}}$ = 3.2, 3.5, 3.8, 3.9, 4.5, 5.2, 6.2, and 7.7 GeV to fill the gap between BES energies and 3 GeV from FXT. In the following sections, we will present the measurements of conserved charge fluctuations from BES-I and FXT 3 GeV data at RHIC.

# 2 Conserved charge fluctuations

## 2.1 Cumulants

Fluctuations of conserved charges are measured in terms of various order of cumulants. The $r$th-order cumulant, $C_r$, is defined by $r$th-derivatives of cumulant generating function [17], which is expressed by moments as: $C_1 = \langle N\rangle$, $C_2 = \langle(\delta N)^2\rangle$, $C_3 = \langle(\delta N)^3\rangle$, $C_4 = \langle(\delta N)^4\rangle - 3\langle(\delta N)^2\rangle^2$, $C_5 = \langle(\delta N)^5\rangle - 10\langle(\delta N)^2\rangle\langle(\delta N)^3\rangle$, $C_6 = \langle(\delta N)^6\rangle + 30\langle(\delta N)^2\rangle^3 - 15\langle(\delta N)^2\rangle\langle(\delta N)^3\rangle$, where $N$ is the number of net-particles of a conserved charge measured within the experimental acceptance and the bracket represents the event average. Another notation, $\langle N^r\rangle_{\rm c} = C_r$, will also be used in following sections, where the subscript c represents the cumulant. Similarly, the 2nd-order mix-cumulant between two conserved quantities can be expressed as: $\langle XY\rangle_{\rm c} = \langle XY\rangle - \langle X\rangle\langle Y\rangle$, where $X$ and $Y$ represent net-particle multiplicities of two different conserved quantities or particle species. The cumulants have a volume dependence by definition. To cancel this trivial effect, we take the ratio between different orders of cumulants, e.g., $C_3/C_2$ and $C_4/C_2$. These ratios can be directly compared with the corresponding susceptibility ratios from theoretical calculations.

## 2.2 Analysis techniques

The event-by-event net-proton multiplicity distributions are shown in Fig. 2 from BES-I [5]. We study the precise structures at the tail of the distributions through the measurements of various order of cumulants. One should keep in mind that these are raw distributions which suffer from the experimental artifacts such as the detector efficiency [18, 19], initial volume fluctuations [20, 21, 22], pileup events [23, 24], and so on.

The effect of the detector efficiencies were corrected by using the correction formulas, which is derived based on the assumption that detector efficiency follows the binomial distribution [25, 26, 19]. The possible deviation from the binomial distribution was studied in embedding simulations at Au+Au 200 GeV most central collisions, where we found that the efficiencies of the STAR detector can be well describe by the beta-binomial distribution [6]. The net-proton $C_4/C_2$ values corrected for the beta-binomial distribution [27] were found to be consistent with those from the binomial efficiency correction within statistical uncertainties, and therefore it was concluded that the efficiency distribution of the STAR detector was close enough to the binomial distribution within the current statistical precision.

In heavy-ion collisions, the number of participant nucleons and particle multiplicity are not one-to-one corresponding, which distorts the cumulants of net-particle distributions. This effect is referred to as initial volume fluctuations. The effect was suppressed by applying the data-driven approach of the Centrality Bin Width Correction (CBWC) [28, 29], where the cumulants were calculated at each reference multiplicity bin and averaged at each centrality class. It was also confirmed that the CBWC gives consistent results with another approach to correct for initial volume fluctuation in an analytical way [30] for the BES-I data sets [6]. It should be noted that the neutrons cannot be measured at the STAR detector. Thus, we measured net-proton distributions as a proxy of net-baryon distributions.

The fraction of pileup events were much higher for 3.0 GeV data from FXT compared to the collider energies from BES-I. We first determined the pileup fraction and the reference multiplicity distributions of the single-collision events by using the unfolding approach [31]. This allowed us to determine the response matrices between single-collision multiplicity and that for the pileup events, which was used for the pileup correction of cumulants [24, 32, 33].

## 2.3 Baselines

Experimentally-measured cumulant ratios of net-proton distributions are compared with the baselines. The simplest case is that the protons and antiprotons follow independent Poisson distributions, respectively. Then the resulting net-proton distribution follows the Skellam distribution, whose odd-order cumulants becomes $\mu_p - \mu_{\bar{p}}$ while even-order cumulants are $\mu_p + \mu_{\bar{p}}$, where $\mu_p$ and $\mu_{\bar{p}}$ denote the mean value of protons and antiprotons. As a result, the $C_4/C_2$ value for the Skellam distribution becomes unity for all collision energies and centralities, and therefore the deviation of the experimental results with respect to unity indicate the effects of the non-statistical fluctuations. It is also important to incorporate the background effects that cannot be avoided in experiments, such as initial volume fluctuations and baryon number conservation [34]. These effects are generally simulated in hadronic transport model, which is employed as a more realistic baseline than

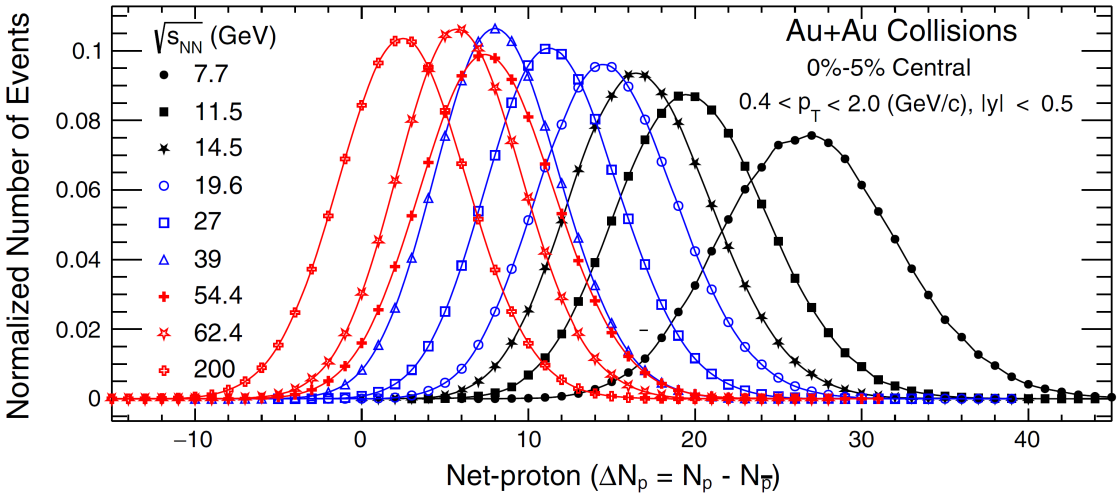


Figure 2: Event-by-event raw net-proton multiplicity distributions for Au+Au collisions at BES-I energies [5].

the Skellam baseline.

# 3 Net-proton fluctuations

## 3.1 $C_4/C_2$ for the critical point search

Figure 3 shows the collision energy dependence of net-proton $C_4/C_2$ in Au+Au most central collisions from BES-I [5, 6] and the FXT program at $\sqrt{s_{\rm NN}} = 3$ GeV [32, 33]. The $C_4/C_2$ value is consistent with the Poisson baseline at $\sqrt{s_{\rm NN}} = 200$ GeV while it decreases with decreasing the collision energy, then take a minimal value at 19.6 GeV. The ratio seems to increase above the Poisson baseline at lower collision energies down to 7.7 GeV. The collision energy dependence was found to have nonmonotonicity of 3.1 $\sigma$. The observed nonmonotonic collision energy dependence is qualitatively consistent with the model calculation incorporating the QCD critical point [35], and therefore the BES-I results could indicate the existence of the critical point at $7.7 \leq \sqrt{s_{\rm NN}} \leq 19.6$ GeV. The proton $C_4/C_2$ values from the HADES experiment at 2.4 GeV [22] and STAR-FXT at 3.0 GeV are also plotted in Fig. 3. They are consistent with each other within uncertainties. The STAR-FXT result can be reproduced by the UrQMD calculations, which indicates that the hadronic interactions are dominant at 3 GeV collisions and the QCD critical point may only exist at $\sqrt{s_{\rm NN}} > 3.0$ GeV. Further conclusion will be made after the completion of the ongoing analysis for the phase II of the BES program (BES-II) and FXT at $3.2 \leq \sqrt{s_{\rm NN}} \leq 27$ GeV [4].

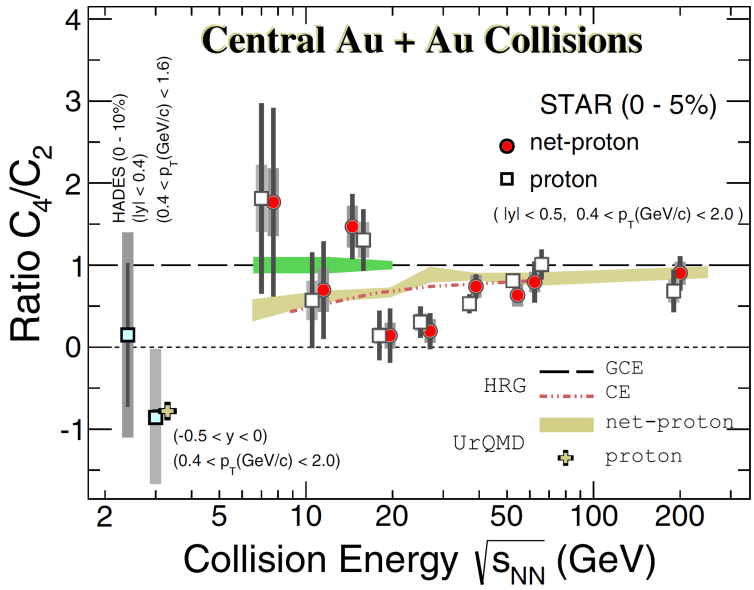


Figure 3: Collision energy dependence of (net-)proton $C_4/C_2$ for Au+Au most central collisions from the BES-I and FXT [32]. The golden band and cross represent the UrQMD calculations. The green band shows the projection of statistical uncertainties for BES-II energies in the collider mode.

### 3.2 $C_6/C_2$ for the crossover search

The STAR experiment also measured further higher-order cumulants up to the sixth order. Theoretically, the net-baryon $C_6/C_2$ is expected to be more sensitive to the QCD phase structure than $C_4/C_2$, as its sign changes near the phase transition temperature [36]. The left panel of Fig. 4 shows the centrality dependence of net-proton $C_6/C_2$ in Au+Au collisions at $\sqrt{s_{\rm NN}} = 27$, 54.4, and 200 GeV [37]. The $C_6/C_2$ values from 27 and 54.4 GeV are consistent with zero within large uncertainties, while those from 200 GeV are progressively negative systematically from peripheral to central collisions. These negative signs are qualitatively consistent with lattice QCD calculations [38]. Thus, the results from 200 GeV could indicate the experimental signature of the smooth crossover at RHIC top energy. The collision energy dependence of (net-)proton $C_6/C_2$ is shown in the right panel in Fig. 4 for Au+Au 0-40% and 50-60% collisions. The $C_6/C_2$ value from 0-40% centrality decreases with decreasing the collision energy down to 7.7 GeV, while it is consistent with UrQMD calculations at 3 GeV. The decreasing trend down to 7.7 GeV is qualitatively consistent with the FRG model down to 7.7 GeV [39] and lattice QCD calculations down to 39 GeV [38], where those calculations include a smooth crossover transition.

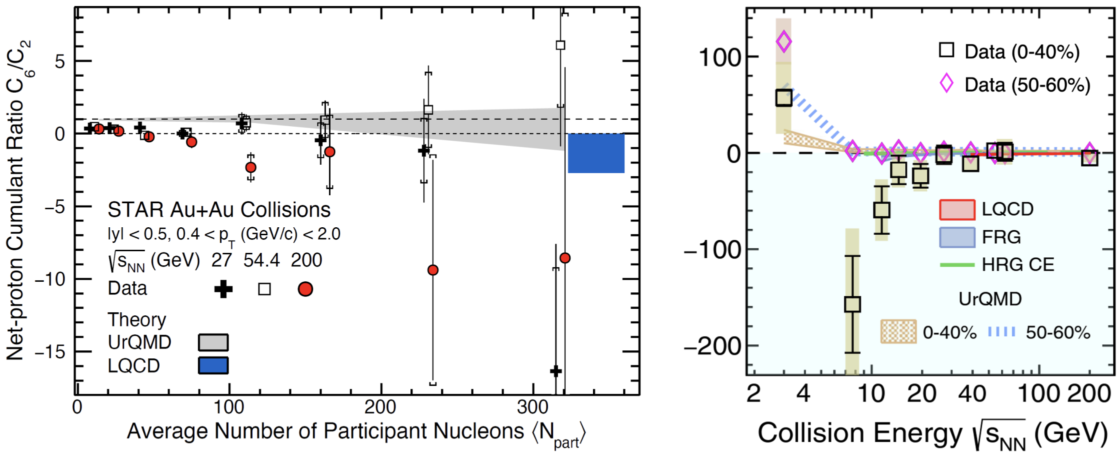


Figure 4: (Left) Centrality dependence of net-proton $C_6/C_2$ at 27, 54.4, and 200 GeV Au+Au collisions [37]. The lattice QCD calculations are from Ref. [38]. (Right) Collision energy dependence of (net-)proton $C_6/C_2$ for Au+Au collisions at 0-40% and 50-60% centralities [40]. The $C_6/C_2$ values for lattice QCD and FRG calculations are from Refs. [38] and [39].

# 4 Challenge for baryon-strangeness correlations

## 4.1 Previous measurement

Correlations between two conserved charges are expected to carry important information on the magnetic field formed in non-central heavy-ion collisions [41] as well as the temperature of the system [42]. Observables suggested by theories consist of the second-order mix-cumulant between net-baryon and net-strangeness, that we call baryon-strangeness correlation in the rest of this article. The importance of the baryon-strangeness correlations was firstly proposed in Ref. [43] in terms of the correlator $C_{BS} = -3\dfrac{\langle BS\rangle_{\rm c}}{\langle S^2\rangle_{\rm c}}$, where $\langle BS\rangle_{\rm c}$ denotes the baryon-strangeness correlation and $\langle S^2\rangle_{\rm c}$ is the 2nd-order net-strangeness cumulant. The $C_{BS}$ value is expected to be unity for the ideal QGP while it strongly depends on the baryon-chemical potential for the hadronic gas. However, the $C_{BS}$ values extracted from previous STAR measurement [44] are between -0.12 and 0.043 for $7.7 \leq \sqrt{s_{\rm NN}} \leq 200$ GeV, which is much smaller than the expectations. According to the model calculations [45], the signal of the baryon-strangeness correlations vanish once the strange baryons (hyperons) are excluded from the measurements. The $C_{BS}$ values were thus very small as only (anti)protons and charged kaons were taken into account as proxies of net-baryon and net-strangeness, respectively, in previous STAR measurements.

To include hyperons in the measurement of event-by-event fluctuations, one has to address the issue of the combinatorial backgrounds. As hyperons decay into daughter particles before hitting the detector, and therefore the invariant mass technique is usually employed to reconstruct hyperons [46]. One can see the signal peak of the hyperons of interest and determine the shape of the combinatorial backgrounds by optimizing the cut conditions for topological parameters for hyperon reconstructions. Then one can subtract the background from the measurement to extract the signal yield and its event average. However, it is impossible to identify signal and background particles on a candidate-by-candidate basis. Hence, the event-by-event fluctuation measurement of hyperons is challenging.

### 4.2 New method: Purity correction

Figure 5 shows a sketch of the invariant mass distribution for $\Lambda$. The shape of the combinatorial backgrounds is assumed to be flat for simplicity. What we can measure in the experiment is always the sum of signal and background particles, $m_{SN} = m_S + m_N$, where $m_{SN}$ is the number of signal candidates, $m_S$ is the signal particles, and $m_N$ is the background particles. It is impossible to identify $m_S$ and $m_N$ on an event-by-event basis. The 2nd-order cumulant of signal candidates is expressed as:

$$\langle m_{SN}^2 \rangle_{\mathrm{c}} = \langle m_S^2 \rangle_{\mathrm{c}} + \langle m_N^2 \rangle_{\mathrm{c}} + 2\langle m_S m_N \rangle_{\mathrm{c}}, \tag{1}$$

thus,

$$\langle m_S^2 \rangle_{\mathrm{c}} = \langle m_{SN}^2 \rangle_{\mathrm{c}} - \langle m_N^2 \rangle_{\mathrm{c}} - 2\langle m_S m_N \rangle_{\mathrm{c}}, \tag{2}$$

where the last two terms on the right-hand side in Eq. (2) cannot be measured experimentally.

Let us consider utilizing the sideband particles around the signal peak as the proxy of the background particles. Sideband particles, $m_{R,i}$, are counted at the $i$th sideband windows indicated by dotted lines in Fig. 5. Supposing that the probability distribution of sideband particles is consistent with that for the background particles, the following relations hold:

$$\begin{aligned} \langle m_N^2 \rangle_{\mathrm{c}} &= \langle m_{R,i}^2 \rangle_{\mathrm{c}}, & (3) \\ \langle m_S m_N \rangle_{\mathrm{c}} &= \langle m_S m_{R,i} \rangle_{\mathrm{c}}, & (4) \\ \langle m_N m_{R,i} \rangle_{\mathrm{c}} &= \langle m_{R,i} m_{R,j} \rangle_{\mathrm{c}}, \quad (i \neq j). & (5) \end{aligned}$$

From Eqs. (2)–(4), we obtain

$$\langle m_S^2 \rangle_{\mathrm{c}} = \langle m_{SN}^2 \rangle_{\mathrm{c}} - \langle m_{R,i}^2 \rangle_{\mathrm{c}} - 2\langle m_S m_{R,i} \rangle_{\mathrm{c}}. \tag{6}$$

Next, we consider the 2nd-order mix-cumulant between signal candidates and sideband

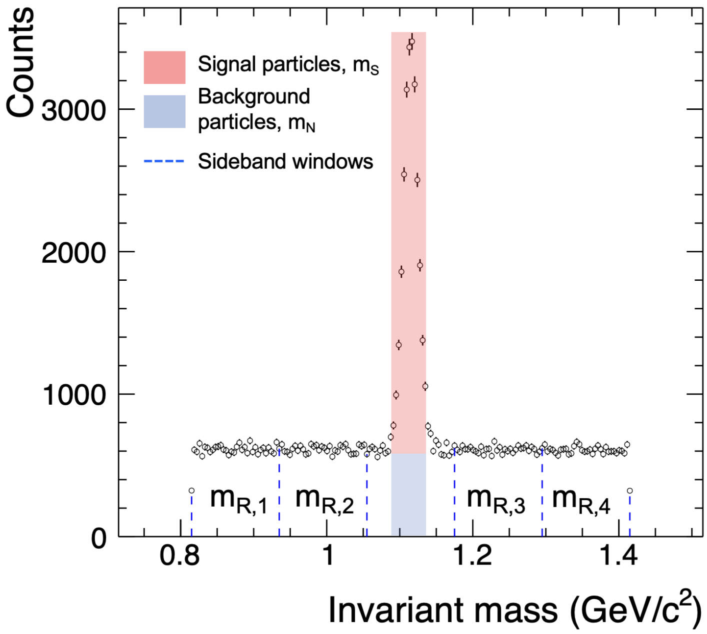


Figure 5: Example of the invariant mass distribution for $\Lambda$. The red shaded area corresponds to the signal particles, and the blue one corresponds to the background particles. The dotted blue lines are the boundaries for the sideband windows.

particles:

$$\langle m_{SN} m_{R,i} \rangle_{\rm c} = \langle m_S m_{R,i} \rangle_{\rm c} + \langle m_N m_{R,i} \rangle_{\rm c} \tag{7}$$

$$= \langle m_S m_{R,i} \rangle_{\rm c} + \langle m_{R,i} m_{R,j} \rangle_{\rm c}, \quad (i \neq j), \tag{8}$$

thus,

$$\langle m_S m_{R,i} \rangle_{\rm c} = \langle m_{SN} m_{R,i} \rangle_{\rm c} - \langle m_{R,i} m_{R,j} \rangle_{\rm c}. \tag{9}$$

From Eq. (7) to Eq. (8) we used Eq. (5). By substituting Eq. (9) to Eq. (6), we obtain the correction formula for the 2nd-order cumulant as

$$\langle m_S^2 \rangle_{\rm c} = \langle m_{SN}^2 \rangle_{\rm c} - \langle m_{R,i}^2 \rangle_{\rm c} - 2\langle m_{SN} m_{R,i} \rangle_{\rm c} + 2\langle m_{R,i} m_{R,j} \rangle_{\rm c}. \tag{10}$$

Similarly, the correction formula for the 2nd-order mix-cumulant can be derived as

$$\langle m_S n_S \rangle_{\rm c} = \langle m_{SN} n_{SN} \rangle_{\rm c} - \langle m_{SN} n_{R,i} \rangle_{\rm c} - \langle n_{SN} m_{R,i} \rangle_{\rm c} + \langle m_{R,i} n_{R,i} \rangle_{\rm c}, \tag{11}$$

where $n$ is supposed to be the other conserved charge or particle species than $m$, and we utilized the following relations:

$$\langle m_S n_N \rangle_{\rm c} \rightarrow \langle m_S n_{R,i} \rangle_{\rm c} = \langle m_{SN} n_{R,i} \rangle_{\rm c} - \langle m_{R,i} n_{R,i} \rangle_{\rm c}, \tag{12}$$

$$\langle m_N n_S \rangle_{\rm c} \rightarrow \langle m_{R,i} n_S \rangle_{\rm c} = \langle m_{R,i} n_{SN} \rangle_{\rm c} - \langle m_{R,i} n_{R,i} \rangle_{\rm c}, \tag{13}$$

$$\langle m_N m_N \rangle_{\rm c} \rightarrow \langle m_{R,i} n_{R,i} \rangle_{\rm c}. \tag{14}$$

It should be noted that the sideband windows need to be determined carefully. Because of the trivial volume dependence, the values of $\langle m_{R,i}^2 \rangle_\mathrm{c}$, $\langle m_{R,i} m_{R,j} \rangle_\mathrm{c}$, and other (mix-)cumulants which include sideband particles can easily change depending on the width of the sideband windows. The purpose of utilizing the sideband windows is to use them as the proxies of the background particles under the signal peak, and therefore the width of the sideband windows have to be precisely determined so that their yields are consistent with the background particles that we want to subtract. This leads to the iterative steps as follows. First, we determine the background yields by data-driven approach like rotation or event-mixing method. Second, we divide the sideband according to the background yields. Finally, we calculate the correction parameters for each window of the sideband.

It is further suggested to check if those correction parameters including sideband particles are flat enough as a function of the invariant mass. Otherwise, one should revisit the definition of the sideband windows to check if the sideband is equally divided. The residual dependence of correction parameters on the invariant mass need to be taken into account as a part of the systematic uncertainties. One can also take the average over as many sideband windows as possible to determine the correction parameters more precisely.

### 4.3 Measurement of $\Lambda$ and $\Xi^-$ hyperons

The $\Lambda$ and $\Xi^-$ hyperons were reconstructed by using the invariant mass technique based on the following decay channels: $\Lambda \to p + \pi^-$ and $\Xi^- \to \Lambda + \pi^-$. The topological parameters such as the distance of the closest approach (DCA) of daughter particles, DCA between daughter particles, DCA and the decay length of hyperons, were optimized so that the signal peak becomes visible. Figure 6 shows the invariant mass ($M_\mathrm{inv}$) distributions for $\Lambda$ and $\Xi^-$, where the clear peaks from $\Lambda$ and $\Xi^-$ are seen around $M_\mathrm{inv} = 1.12$ GeV/c$^2$ and 1.32 GeV/c$^2$, respectively. Another peak around 1.28 GeV/c$^2$ in $\Xi^-$ invariant mass distribution is the fake signal which appears if the bachelor $\pi^-$ are daughters from $\Lambda$. This fake signal does not affect our measurement. The background shape was determined by using the rotation method, which is shown by cyan solid lines in Fig. 6. The yield of the background particles were then estimated from the rotational backgrounds, based on which the sidebands are equally divided (sideband windows), as shown by magenta dotted lines.

The signal candidates for $\Lambda$ and $\Xi^-$ were counted at $1.11 < M_\mathrm{inv} < 1.12$ GeV/c$^2$ and $1.32 < M_\mathrm{inv} < 1.33$ GeV/c$^2$, respectively, on an event-by-event basis. Sideband particles were counted at each sideband window in Fig. 6. Figure 7 shows the 1st- and 2nd-order cumulants of sideband particles, and the 2nd-order mix-cumulant between signal candidates and sideband particles, as a function of invariant mass. The 1st-order cumulant is

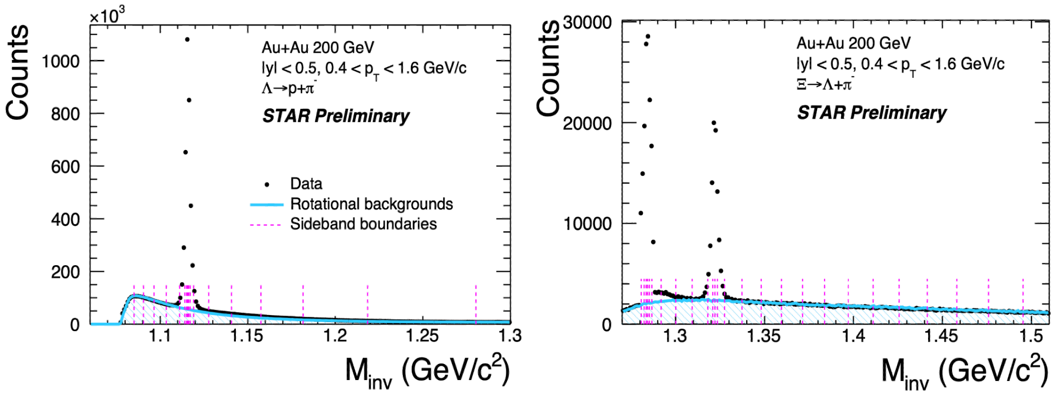


Figure 6: Invariant mass distribution of $\Lambda$ (left) and $\Xi^-$ (right) hyperons. The cyan solid lines represent the rotation backgrounds, and the magenta dotted lines are the sideband boundaries for the purity corrections.

flat by definition, as the sideband was equally divided based on the background yields. It is found that the 2nd-order cumulants and mix-cumulants are also flat as well, which indicates that the parameters for the purity correction do not depend on the invariant mass, and those sideband particles can be used as proxies of the background particles under the signal peak.

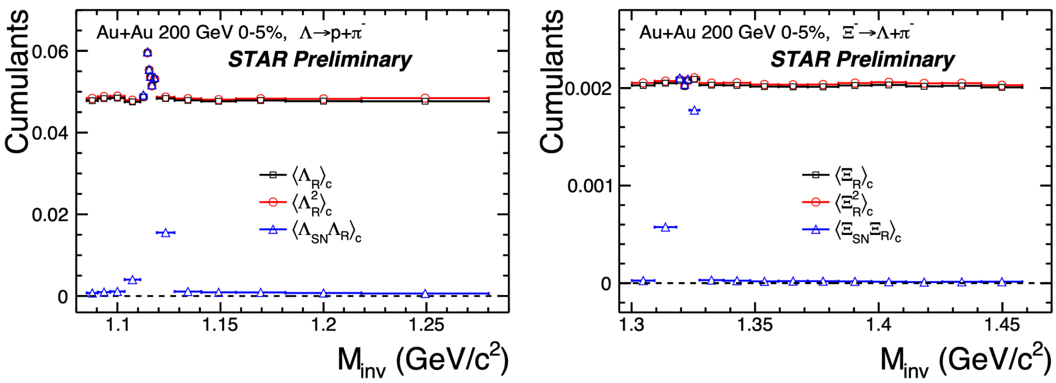


Figure 7: The 1st- and 2nd-order cumulants of sideband particles, $\langle\Lambda_R\rangle_c$ and $\langle\Lambda_R^2\rangle_c$ (the subscript $R$ represents the rotational backgrounds), and the 2nd-order mix-cumulants between signal candidates and sideband particles, $\langle\Lambda_{SN}\Lambda_R\rangle_c$, for $\Lambda$ (left) and $\Xi^-$ (right).

The analysis of the $C_{BS}$ was performed for two cases: (1) Measure $\Lambda$ and $\bar{\Lambda}$ on top of $p$, $\bar{p}$, and $K^{\pm}$, (2) Add $\Xi^-$ and $\bar{\Xi}^+$ on top of (1). The baryon-strangeness correlation and the 2nd-order strangeness cumulant are given by

$$\langle BS\rangle_c = \langle\Delta p\Delta K\rangle_c - \langle\Delta p\Delta\Lambda\rangle_c + \langle\Delta\Lambda\Delta K\rangle_c - \langle\Delta K^2\rangle_c, \tag{15}$$

$$\langle S^2\rangle_c = \langle\Delta K^2\rangle_c + \langle\Delta\Lambda^2\rangle_c - 2\langle\Delta K\Delta\Lambda\rangle_c, \tag{16}$$

for case (1), and

$$\begin{aligned}\langle BS\rangle_{\rm c} &= \langle\Delta p\Delta K\rangle_{\rm c} - \langle\Delta p\Delta\Lambda\rangle_{\rm c} - 2\langle\Delta\Xi\rangle_{\rm c} + \langle\Delta\Lambda\Delta K\rangle_{\rm c} - \langle\Delta K^2\rangle_{\rm c} \\ &\quad -3\langle\Delta\Lambda\Delta\Xi\rangle_{\rm c} + \langle\Delta\Xi\Delta K\rangle_{\rm c} - 2\langle\Delta\Xi^2\rangle_{\rm c}, \qquad (17) \\ \langle S^2\rangle_{\rm c} &= \langle\Delta K^2\rangle_{\rm c} + \langle\Delta\Lambda^2\rangle_{\rm c} + 4\langle\Delta\Xi^2\rangle_{\rm c} - 2\langle\Delta K\Delta\Lambda\rangle_{\rm c} - 4\langle\Delta K\Delta\Xi\rangle_{\rm c} \\ &\quad +4\langle\Delta\Lambda\Delta\Xi\rangle_{\rm c}, \qquad (18)\end{aligned}$$

for case (2), where $\Delta X$ represents the difference between number of particles and antiparticles of a particle species $X$. The coefficients in front of $\Xi$-related terms come from the fact that $\Xi$ hyperons carry two strange quarks. To obtain $\langle BS\rangle_{\rm c}$ and $\langle S^2\rangle_{\rm c}$, all the 2nd-order cumulants and mix-cumulants in Eqs. (15)–(18) were measured with efficiency corrections. Hyperons-related terms were corrected for their purities as well.

### 4.4 Results

The validity of the purity correction was checked in a data-driven way by analyzing the various topological cut sets for $\Lambda$ reconstructions. Each cut set has different purity [1] and significance [2] of $\Lambda$. The efficiency and purity corrected value of the $\Lambda$ fluctuations should be consistent among different cut sets if the purity correction works well. Figure 8 shows the 2nd-order $\Lambda$ cumulant from Au+Au most central collisions at $\sqrt{s_{\rm NN}} = 200$ GeV as a function of $\Lambda$ purity, where purity-uncorrected results are shown by black squares and purity-corrected results are shown by red circles. The purity-uncorrected results increase with decreasing the purity because the background contribution becomes large. In this case, the result having the highest purity around 96% can only be taken as a final result which still suffers from 4% background contributions. After applying purity corrections for each cut set, the results are flat with respect to the purity and seem crossing with the purity-uncorrected results at the highest purity. This indicates that the purity correction works well in the STAR data. More importantly, one can take any of the red circles as a final result. We finally employed the result from the cut set which yields the best significance of $\Lambda$, leading to the smallest statistical uncertainty of purity-corrected $\langle\Lambda^2\rangle_c$.

Figure 9 shows the centrality dependence of $C_{BS}$ from Au+Au 200 GeV collisions. The results are corrected for purity and reconstruction efficiency, while not corrected for hyperons' branching ratio. The $C_{BS}$ values have been significantly enhanced compared to the previous measurement [44] by including $\Lambda$ and $\bar{\Lambda}$ on top of $p$, $\bar{p}$, and $K^{\pm}$, as shown by blue squares. We have also tried including multi-strange baryons $\Xi^-$ and $\bar{\Xi}^+$ as well,

[1] The ratio of the signal to the background yields.

[2] The ratio of the signal yield to the square-root of signal candidates, which is a proxy for the product of purity and reconstruction efficiency.

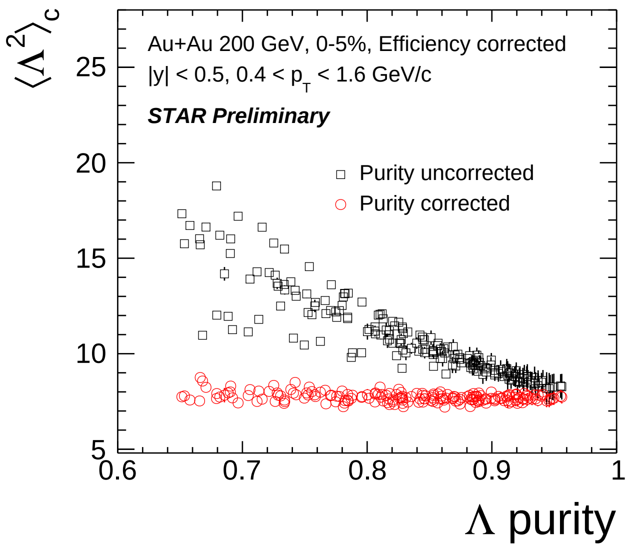


Figure 8: The 2nd-order $\Lambda$ cumulant as a function of $\Lambda$ purity from Au+Au most central collisions at 200 GeV. Purity-uncorrected results are shown by black squares, and purity-corrected results are shown by red circles. All results are corrected for reconstruction efficiencies. The branching ratio is not taken into account.

which is shown by red stars. A slightly different centrality dependence is observed for both cases. The $C_{BS}$ values are much closer to those from the lattice QCD calculations [47] shown by the purple band than previous measurement. The red and blue shaded bands represent the UrQMD calculations incorporating $\Sigma^0$ as well as the particle species in the experimental measurements. The $\Sigma^0$ decays into $\Lambda$ and $\gamma$ and the daughter $\Lambda$s are already included in our measurements. The UrQMD calculations significantly underestimate the experimental data and cannot describe the centrality dependence.

## 5 Summary

We discussed the recent results on conserved charge fluctuations from BES-I and $\sqrt{s_{\mathrm{NN}}} = 3$ GeV collisions from FXT program at RHIC. The nonmonotonic energy dependence of (net-)proton $C_4/C_2$ could hint on the existence of the QCD critical point around $7.7 \leq \sqrt{s_{\mathrm{NN}}} \leq 19.6$ GeV. The negative signs observed in net-proton $C_6/C_2$ at 200 GeV could indicate the experimental signature of a smooth crossover at RHIC top energy. The collision energy dependence of (net-)proton $C_6/C_2$ could imply that the phase boundary can be probed over the wide range of the QCD phase diagram. These interpretations are currently limited due to large uncertainties, which will be significantly improved in the near future by the ongoing analysis on BES-II data having 10-20 times larger event

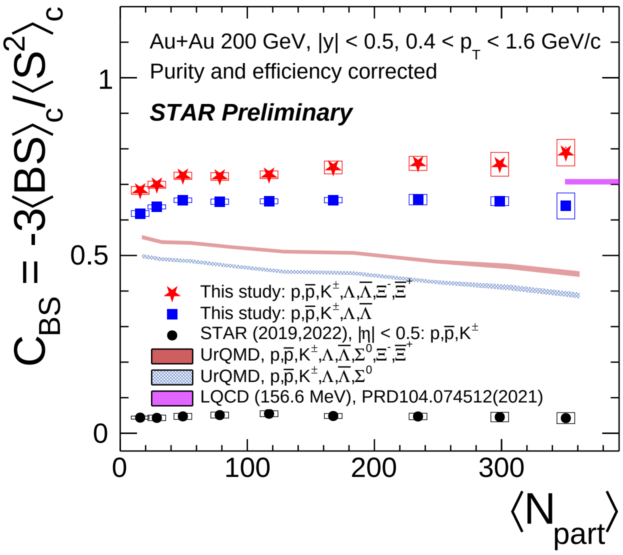


Figure 9: Centrality dependence of $C_{BS}$ from Au+Au 200 GeV collisions. The results are corrected for purity and reconstruction efficiencies for hyperons, while their branching ratios are not taken into account. The purple band represents the results from the lattice QCD calculations [47]. The UrQMD calculations are shown by red and blue shaded bands.

statistics compared to BES-I. We also reported the recent attempt for measuring the baryon-strangeness correlations. The $\Lambda$, $\Xi^-$, and their antiparticles were included in the measurement, on top of $p$, $\bar{p}$, and $K^{\pm}$. The results were corrected for the combinatorial backgrounds by using the newly-developed method for the purity correction. The validity of the correction was confirmed in a data-driven way. As a result, the $C_{BS}$ values were significantly enhanced and the value is now much closer to the lattice QCD calculations.

# Acknowledgments

This work was supported by JSPS KAKENHI Grant No. 23K13113 and 19H05598.

# References

[1] Adam Bzdak et al. Mapping the Phases of Quantum Chromodynamics with Beam Energy Scan. *Phys. Rept.*, 853:1–87, 2020.

[2] Y. Aoki et al. The Order of the quantum chromodynamics transition predicted by the standard model of particle physics. *Nature*, 443:675–678, 2006.

[3] Shinji Ejiri. Canonical partition function and finite density phase transition in lattice QCD. *Phys. Rev. D*, 78:074507, 2008.

[4] Studying the phase diagram of qcd matter at rhic. https://drupal.star.bnl.gov/STAR/starnotes/public/sn0598.

[5] J. Adam et al. Nonmonotonic Energy Dependence of Net-Proton Number Fluctuations. *Phys. Rev. Lett.*, 126(9):092301, 2021.

[6] Mohamed Abdallah et al. Cumulants and correlation functions of net-proton, proton, and antiproton multiplicity distributions in Au+Au collisions at energies available at the BNL Relativistic Heavy Ion Collider. *Phys. Rev. C*, 104(2):024902, 2021.

[7] L. Adamczyk et al. Beam energy dependence of moments of the net-charge multiplicity distributions in Au+Au collisions at RHIC. *Phys. Rev. Lett.*, 113:092301, 2014.

[8] L. Adamczyk et al. Collision Energy Dependence of Moments of Net-Kaon Multiplicity Distributions at RHIC. *Phys. Lett. B*, 785:551–560, 2018.

[9] L. Adamczyk et al. Beam-Energy Dependence of the Directed Flow of Protons, Antiprotons, and Pions in Au+Au Collisions. *Phys. Rev. Lett.*, 112(16):162301, 2014.

[10] L. Adamczyk et al. Bulk Properties of the Medium Produced in Relativistic Heavy-Ion Collisions from the Beam Energy Scan Program. *Phys. Rev. C*, 96(4):044904, 2017.

[11] L. Adamczyk et al. Observation of an Energy-Dependent Difference in Elliptic Flow between Particles and Antiparticles in Relativistic Heavy Ion Collisions. *Phys. Rev. Lett.*, 110(14):142301, 2013.

[12] L. Adamczyk et al. Elliptic flow of identified hadrons in Au+Au collisions at $\sqrt{s_{NN}} =$ 7.7-62.4 GeV. *Phys. Rev. C*, 88:014902, 2013.

[13] L. Adamczyk et al. Beam Energy Dependence of Jet-Quenching Effects in Au+Au Collisions at $\sqrt{s_{\rm NN}}$ = 7.7, 11.5, 14.5, 19.6, 27, 39, and 62.4 GeV. *Phys. Rev. Lett.*, 121(3):032301, 2018.

[14] B. I. Abelev et al. Azimuthal Charged-Particle Correlations and Possible Local Strong Parity Violation. *Phys. Rev. Lett.*, 103:251601, 2009.

[15] B. I. Abelev et al. Observation of charge-dependent azimuthal correlations and possible local strong parity violation in heavy ion collisions. *Phys. Rev. C*, 81:054908, 2010.

[16] M. I. Abdulhamid et al. Measurements of dielectron production in Au+Au collisions at sNN=27, 39, and 62.4 GeV from the STAR experiment. *Phys. Rev. C*, 107(6):L061901, 2023.

[17] Masayuki Asakawa and Masakiyo Kitazawa. Fluctuations of conserved charges in relativistic heavy ion collisions: An introduction. *Prog. Part. Nucl. Phys.*, 90:299–342, 2016.

[18] Toshihiro Nonaka et al. More efficient formulas for efficiency correction of cumulants and effect of using averaged efficiency. *Phys. Rev.*, C95(6):064912, 2017.

[19] Xiaofeng Luo and Toshihiro Nonaka. Efficiency correction for cumulants of multiplicity distributions based on track-by-track efficiency. *Phys. Rev. C*, 99(4):044917, 2019.

[20] V. Skokov et al. Volume Fluctuations and Higher Order Cumulants of the Net Baryon Number. *Phys. Rev.*, C88:034911, 2013.

[21] Tetsuro Sugiura et al. Volume fluctuation and multiplicity correlation in higher-order cumulants. *Phys. Rev.*, C100(4):044904, 2019.

[22] J. Adamczewski-Musch et al. Proton-number fluctuations in $\sqrt{s_{NN}}$ =2.4 GeV Au + Au collisions studied with the High-Acceptance DiElectron Spectrometer (HADES). *Phys. Rev. C*, 102(2):024914, 2020.

[23] P. Garg and D.K. Mishra. Higher moments of net-proton multiplicity distributions in a heavy-ion event pile-up scenario. *Phys. Rev. C*, 96(4):044908, 2017.

[24] Toshihiro Nonaka et al. Pileup corrections on higher-order cumulants. *Nucl. Instrum. Meth. A*, 984:164632, 2020.

[25] Xiaofeng Luo. Unified Description of Efficiency Correction and Error Estimation for Moments of Conserved Quantities in Heavy-Ion Collisions. *Phys. Rev.*, C91(3):034907, 2015.

[26] Masakiyo Kitazawa and Xiaofeng Luo. Properties and uses of factorial cumulants in relativistic heavy-ion collisions. *Phys. Rev.*, C96(2):024910, 2017.

[27] ShinIchi Esumi et al. Reconstructing particle number distributions with convoluting volume fluctuations. *Nucl. Instrum. Meth. A*, 987:164802, 2021.

[28] Xiaofeng Luo et al. Volume fluctuation and auto-correlation effects in the moment analysis of net-proton multiplicity distributions in heavy-ion collisions. *J. Phys.*, G40:105104, 2013.

[29] Xiaofeng Luo and Nu Xu. Search for the QCD Critical Point with Fluctuations of Conserved Quantities in Relativistic Heavy-Ion Collisions at RHIC : An Overview. *Nucl. Sci. Tech.*, 28(8):112, 2017.

[30] P. Braun-Munzinger et al. Bridging the gap between event-by-event fluctuation measurements and theory predictions in relativistic nuclear collisions. *Nucl. Phys.*, A960:114–130, 2017.

[31] Yu Zhang, Yige Huang, Toshihiro Nonaka, and Xiaofeng Luo. Pileup correction on higher-order cumulants with unfolding approach. *Nucl. Instrum. Meth. A*, 1026:166246, 2022.

[32] M. S. Abdallah et al. Measurements of Proton High Order Cumulants in $\sqrt{s_{\mathrm{NN}}}$ = 3 GeV Au+Au Collisions and Implications for the QCD Critical Point. *Phys. Rev. Lett.*, 128(20):202303, 2022.

[33] Mohamed Abdallah et al. Higher-order cumulants and correlation functions of proton multiplicity distributions in sNN=3 GeV Au+Au collisions at the RHIC STAR experiment. *Phys. Rev. C*, 107(2):024908, 2023.

[34] Adam Bzdak, Volker Koch, and Vladimir Skokov. Baryon number conservation and the cumulants of the net proton distribution. *Phys. Rev. C*, 87(1):014901, 2013.

[35] Misha A. Stephanov, K. Rajagopal, and Edward V. Shuryak. Event-by-event fluctuations in heavy ion collisions and the QCD critical point. *Phys. Rev.*, D60:114028, 1999.

[36] B. Friman et al. Fluctuations as probe of the QCD phase transition and freeze-out in heavy ion collisions at LHC and RHIC. *Eur. Phys. J.*, C71:1694, 2011.

[37] Mohamed Abdallah et al. Measurement of the Sixth-Order Cumulant of Net-Proton Multiplicity Distributions in Au+Au Collisions at $\sqrt{s_{NN}}$ = 27, 54.4, and 200 GeV at RHIC. *Phys. Rev. Lett.*, 127:262301, 2021.

[38] A. Bazavov et al. Skewness, kurtosis, and the fifth and sixth order cumulants of net baryon-number distributions from lattice QCD confront high-statistics STAR data. *Phys. Rev. D*, 101(7):074502, 2020.

[39] Wei-jie Fu, Xiaofeng Luo, Jan M. Pawlowski, Fabian Rennecke, Rui Wen, and Shi Yin. Hyper-order baryon number fluctuations at finite temperature and density. *Phys. Rev. D*, 104(9):094047, 2021.

[40] Bassam Aboona et al. Beam Energy Dependence of Fifth and Sixth-Order Net-proton Number Fluctuations in Au+Au Collisions at RHIC. *Phys. Rev. Lett.*, 130(8):082301, 2023.

[41] H. T. Ding, S. T. Li, Q. Shi, and X. D. Wang. Fluctuations and correlations of net baryon number, electric charge and strangeness in a background magnetic field. *Eur. Phys. J. A*, 57(6):202, 2021.

[42] A. Bazavov et al. Strangeness at high temperatures: from hadrons to quarks. *Phys. Rev. Lett.*, 111:082301, 2013.

[43] V. Koch, A. Majumder, and J. Randrup. Baryon-strangeness correlations: A Diagnostic of strongly interacting matter. *Phys. Rev. Lett.*, 95:182301, 2005.

[44] Jaroslav Adam et al. Collision-energy dependence of second-order off-diagonal and diagonal cumulants of net-charge, net-proton, and net-kaon multiplicity distributions in Au + Au collisions. *Phys. Rev. C*, 100(1):014902, 2019. [Erratum: Phys.Rev.C 105, 029901 (2022)].

[45] Zhenzhen Yang, Xiaofeng Luo, and Bedangadas Mohanty. Baryon-Strangeness Correlations in Au+Au Collisions at $\sqrt{s_{\mathrm{NN}}}$=7.7-200 GeV from the UrQMD model. *Phys. Rev. C*, 95(1):014914, 2017.

[46] Jaroslav Adam et al. Strange hadron production in Au+Au collisions at $\sqrt{s_{NN}}$ =7.7 , 11.5, 19.6, 27, and 39 GeV. *Phys. Rev. C*, 102(3):034909, 2020.

[47] D. Bollweg, J. Goswami, O. Kaczmarek, F. Karsch, Swagato Mukherjee, P. Petreczky, C. Schmidt, and P. Scior. Second order cumulants of conserved charge fluctuations revisited: Vanishing chemical potentials. *Phys. Rev. D*, 104(7), 2021.